

Multi-omics analysis reveals immune features associated with immunotherapy benefit in squamous cell lung cancer patients from Phase III Lung-MAP S1400I trial

Edwin Roger Parra^{1*}, Jiexin Zhang^{2*}, Dzifa Yawa Duose^{1*}, Edgar Gonzalez-Kozlova^{3,4,5,6*}, Mary W. Redman⁷, Hong Chen⁸, Ganiraju C Manyam², Gayatri Kumar¹, Jianhua Zhang⁹, Xingzhi Song⁹, Rossana Lazcano¹, Mario L. Marques-Piubelli¹, Caddie Laberiano-Fernandez¹, Frank Rojas¹, Baili Zhang¹, Len Taing¹⁰, Aashna Jhaveri¹⁰, Jacob Geisberg¹⁰, Jennifer Altreuter¹⁰, Franziska Michor¹⁰, James Provencher¹⁰, Joyce Yu¹⁰, Ethan Cerami¹⁰, Radim Moravec¹¹, Kasthuri Kannan¹, Rajyalakshmi Luthra¹², Gheath Alatrash¹³, Hsin-Hui Huang^{5,14}, Hui Xie⁵, Manishkumar Patel¹⁵, Kai Nie⁵, Jocelyn Harris⁵, Kimberly Argueta⁵, James Lindsay¹⁵, Roshni Biswas¹⁵, Stephen Van Nostrand^{10,15}, Seunghee Kim-Schulze^{3,4,5,6}, Jhanelle E. Gray¹⁶, Roy Herbst¹⁷, Ignacio I. Wistuba¹, Scott Gettinger¹⁶, Karen Kelly¹⁸, Lyudmila Bazhenova¹⁹, Sacha Gnjjatic^{3,4,5,6}, J. Jack Lee²⁰, Jianjun Zhang^{8,9#}, Cara Haymaker^{1#}

¹Departments of Translational Molecular Pathology, The University of Texas MD Anderson Cancer Center, Houston, TX.

² Department of Bioinformatics & Computational Biology, The University of Texas MD Anderson Cancer Center, Houston, TX.

³Department of Oncological Sciences, Mount Sinai, New York, NY

⁴Tisch Cancer Institute, Mount Sinai, New York, NY

⁵Precision Immunology Institute, Mount Sinai, New York, NY

⁶Icahn School of Medicine at Mount Sinai, New York, NY

⁷SWOG Statistical Center; Fred Hutchinson Cancer Research Center, Seattle, WA.

⁸Department of Thoracic-Head and Neck Medical Oncology, The University of Texas MD Anderson Cancer Center, Houston, TX.

⁹Department of Genomic Medicine, The University of Texas MD Anderson Cancer Center, Houston, TX.

¹⁰CIMAC-CIDC Network, Pipeline development and Portal integration, Dana-Farber Cancer Institute, Boston, MA.

¹¹Cancer Diagnosis Program, Division of Cancer Treatment and Diagnosis, NCI, Bethesda, MD.

¹²Department of Hematopathology, The University of Texas MD Anderson Cancer Center, Houston, TX.

¹³Department of Stem Cell Transplantation, The University of Texas MD Anderson Cancer,

¹⁴Department of Population Health Science & Policy, Icahn School of Medicine at Mount Sinai.

¹⁵Department of Data Science, Dana-Farber Cancer Institute, Boston, MA.

¹⁶Moffitt Cancer Center, Tampa, FL.

¹⁷Yale Cancer Center, Yale School of Medicine, New Haven, CT.

¹⁸International Association for the Study of Lung Cancer, Denver, CO

¹⁹University of California San Diego Moores Cancer Center, La Jolla, CA.

²⁰Department of Biostatistics, The University of Texas MD Anderson Cancer Center, Houston, TX.

*Co-first authors

Co-corresponding authors

Corresponding authors:

Jianjun Zhang

1881 East Road, 3SCR6.3402

Unit 1954

Houston, TX 77054

(t) 713-563-6096

JZhang20@mdanderson.org

Cara Haymaker

7435 Fannin St, 2SCR2.3025

Unit 954

Houston, TX 77054

(t) 713-792-1458

chaymaker@mdanderson.org

Running title: Immune features may predict immunotherapy benefit in SqNSCLC

Keywords: Multi-omics analysis, immune checkpoint inhibitors, cellular distribution, translational study, lung squamous cell carcinoma

Disclosures:

Dzifa Yawa Duose report that has received honoraria from Chrysalis Biomedical. Ignacio I. Wistuba has provided consulting or advisory roles for AstraZeneca/MedImmune, Bayer, Bristol-Myers Squibb, Genentech/Roche, GlaxoSmithKline, Guardant Health, HTG Molecular Diagnostics, Merck, MSD Oncology, OncoCyte, Jansen, Novartis, Flame Inc, Regeneron, Merus, and Pfizer; has received grants and personal fees from Genentech/Roche, Bristol Myers Squibb, AstraZeneca/MedImmune, HTG Molecular, Merck, and Guardant Health; has received personal fees from GlaxoSmithKline and Oncocyte, Daiichi-Sankyo, Roche, Astra Zeneca, Regeneron, Sanofi, Pfizer and Bayer; has received research funding to his institution from 4D Molecular Therapeutics, Adaptimmune, Adaptive Biotechnologies, Akoya Biosciences , Amgen, Bayer, EMD Serono, Genentech, Guardant Health, HTG Molecular Diagnostics, Iovance Biotherapeutics, Johnson & Johnson, Karus Therapeutics, MedImmune, Merck, Novartis, OncoPlex Diagnostics, Pfizer, Takeda, and Novartis. Scott Gettinger declare has received research funding from BMS, NextCure, Genentech, Iovance and Merck. He is safety board from BMS and Iovance Clinical trial's steering committee. Sacha Gnjatic reports other research funding from Boehringer-Ingelheim, Bristol-Myers Squibb, Celgene, Genentech, Regeneron, and Takeda. Lyudmila Bazhenova report a consulting or advisory role of Genentech/Roche, Regeneron, Merck, Johnson and Johnson, Daichi, Neuvogen, Bayer, Sanofi, ORCIC, Novocure, Mirati Therapeutics, Turning Point Therapeutics, Abbvie, InterVenn Biosciences, and Elevation Oncology. Jianjun Zhang reports grant from Merck, grants and personal fees from Johnson and Johnson and Novartis, personal fees from Bristol Myers Squibb, AstraZeneca, GenePlus, Innovent and Hengrui outside the submitted work. Cara Haymaker reports research funding to institution from Sanofi, Dragonfly, BTG, Trisalus, Iovance, and Avenge; scientific advisory board member of Briacell with stock options; personal fees from Nanobiotix and speaker fees/honorarium from SWOG and SITC outside the scope of the submitted work. All other authors declare no potential conflict of interest.

Abstract

Background: Identifying molecular and immune features to guide immune checkpoint inhibitor (ICI)-based regimens remains an unmet clinical need.

Methods: Tissue and longitudinal blood specimens from phase III trial S1400I in metastatic lung squamous cell carcinoma (SqNSCLC) patients treated with nivolumab monotherapy (nivo) or nivolumab plus ipilimumab (nivo+ipi) were subjected to multi-omics analyses including multiplex immunofluorescence (mIF), nCounter PanCancer Immune Profiling Panel, whole-exome sequencing, and Olink.

Results: Higher immune scores from immune gene expression profiling or immune cell infiltration by mIF were associated with response to ICIs and improved survival, except regulatory T cells, which were associated with worse overall survival (OS) for patients receiving nivo+ipi. Immune cell density and closer proximity of CD8+GZB+ T cells to malignant cells were associated with superior progression-free survival (PFS) and OS. The cold immune landscape of NSCLC was associated with a higher level of chromosomal copy number variation (CNV) burden. Patients with *LRP1B*-mutant tumors had a shorter survival than patients with *LRP1B*-wild-type tumors. Olink assays revealed soluble proteins such as LAMP3 increased in responders while IL-6 and CXCL13 increased in nonresponders. Upregulation of serum CXCL13, MMP12, CSF-1, and IL-8 were associated with worse survival before radiologic progression.

Conclusions: The frequency, distribution and clustering of immune cells relative to malignant ones can impact ICI efficacy in SqNSCLC patients. High CNV burden may contribute to the cold immune microenvironment. Soluble inflammation/immune-related proteins in the blood have the potential to monitor therapeutic benefit from ICI treatment in SqNSCLC patients.

Translational Relevance

Identifying molecular and immune features to guide immune checkpoint inhibitor (ICI) regimens remains an unmet clinical need. We performed multi-omics analysis of biospecimens from a phase III trial LUNG-MAP S1400I that compared ipilimumab combined with nivolumab vs. nivolumab monotherapy in patients with metastatic lung squamous cell carcinoma. An overall cold tumor immune microenvironment correlated with high chromosomal copy number variant burden and was associated with inferior benefit from ICIs. In addition to the immune cell density, the proximity and local neighborhood clustering of a subset of immune cells to tumor cells also impacted the benefit from ICI therapy. Interestingly, patient survival was decreased with *LRP1B*-mutant tumors, but not with *LRP1B*-wild type tumors. Many soluble proteins related to inflammation or T-cell and dendritic cell activation correlated with clinical outcome from ICI therapy. Together, these immune features highlight the potential of biomarker-based strategies to select patients for ICI-based regimens and dynamically monitor their response.

Introduction

Immune checkpoint inhibitors (ICIs) targeting programmed cell death protein 1 (PD-1, e.g., nivolumab, pembrolizumab, cemiplimab) or its ligand PD-L1 (e.g., atezolizumab) have become pillars of treatment in both frontline and salvage settings for patients with advanced non–small cell lung cancer (NSCLC) (1-4). In addition, recent efforts have led to multiple approved frontline regimens incorporating chemotherapy and other ICIs with anti–PD-1/PD-L1 antibodies (5-8). However, in the salvage setting, anti–PD-1/PD-L1 monotherapy remains the treatment of choice for ICI-naïve advanced-stage NSCLC (9,10).

Ipilimumab is an ICI targeting cytotoxic T lymphocyte–associated protein 4 (CTLA-4). Its dual inhibition with PD-1/PD-L1 may have synergistic effects on the anticancer immune response, given the complementary functions of these two pathways. The combination of nivolumab with ipilimumab was demonstrated to have superior efficacy than nivolumab alone in patients with advanced melanoma (11,12). For patients with metastatic NSCLC, ipilimumab plus nivolumab has been approved by the US Food and Drug Administration by the US Food and Drug Administration in the frontline setting with or without concurrent chemotherapy (7,8,13,14). In the salvage setting, a recent phase III study, S1400I, evaluated the efficacy of nivolumab plus ipilimumab vs. nivolumab monotherapy in patients without previous ICI treatment for squamous NSCLC (SqNSCLC) (15). The study did not show that ipilimumab plus nivolumab improved clinical outcomes. However, progression-free survival (PFS) and overall survival (OS) curves separated during later follow-up, suggesting that a subset of patients may benefit from combination treatment with ipilimumab and nivolumab.

Understanding the mechanisms underlying response and resistance to ICIs and establishing predictive molecular and immune features to identify patients who will benefit the most from ICI therapy remain unmet clinical needs. High PD-L1 expression is associated with improved outcomes in patients receiving ICI monotherapy (1,8). However, the geographical heterogeneity of PD-L1 expression between primary tumors and metastatic sites and even between different regions within the same tumors—as well as the potential dynamic changes in PD-L1 expression over time—have raised questions about its reliability as a predictive biomarker (16,17). Although tumor mutational burden (TMB) has been approved as a predictive marker for anti–PD-1/PD-L1 treatment for melanoma and NSCLC, and several other cancer types (18), one study found no correlation between TMB or PD-L1 with anti–PD-1 plus anti–

CTLA-4 therapy in patients with NSCLC (19). Furthermore, the predictive value of PD-L1 and TMB becomes less clear when chemotherapy is added. These findings underscore the complexity of molecular determinates of the tumor immune microenvironment and response to ICIs.

In this study, we sought to elucidate the immune and molecular mechanisms that affect benefit from ICIs in patients with advanced SqNSCLC. Toward this end, we integrated immune and multi-omics profiling platforms supported by Cancer Immune Monitoring and Analysis Centers (CIMAC) in the current study. Specifically, we performed multiplex immunofluorescence (mIF), gene expression profiling (ncounter PanCancer Immune Profiling Panel), whole-exome sequencing (WES), and Olink proteomics on tissue and blood specimens from the S1400I trial to identify molecular or immune factors associated with better prognoses in patients treated with anti-PD-1 monotherapy vs. anti-PD-1/CTLA-4 dual combination.

Material and Methods

Study population and human tissue samples

Lung-MAP (S1400I, NCT02785952) was a multicenter, open-label, phase III randomized clinical trial. The substudy Lung-MAP-I (S1400I) was conducted from December 18, 2015, to April 23, 2018, through the National Clinical Trials Network and led by the SWOG Cancer Research Network. The study was conducted in accordance with the Declaration of Helsinki and the Lung-MAP design has been described previously (15). Briefly, the trial compared nivolumab plus ipilimumab (nivo+ipi) with nivolumab monotherapy (nivo) in patients with chemotherapy-pretreated, immunotherapy-naïve, advanced sqNSCLC. Two hundred fifty-two patients were randomly assigned to receive nivo+ipi (n = 125) or nivo (n = 127). The clinical efficacy endpoints were OS, PFS, duration of response, and best objective response by RECIST 1.1. Each site required approval by the US National Cancer Institute central institutional review board or approval by their local institutional review board. Written, informed consent was required for all patients prior to registration.

Available tumor tissue samples and blood samples (N = 160, **Supplementary Figure 1**) submitted for Lung-MAP screening were provided by the SWOG tissue bank. The clinical information for correlative studies in collaboration with the CIMAC–Cancer Immunologic Data Commons (CIDC) Network are shown in **Supplementary Table 1** across the different assays.

Multiplex immunofluorescence staining and analysis

Multiplex immunofluorescence (mIF) staining was performed in 82 screening tumor tissue samples (nivo+ipi = 38, and nivo = 42), (**Supplementary Table 1**). Unstaining slides from formalin-fixed, paraffin-embedded (FFPE) tissue were received from the SWOG bank and stained using methods previously described and validated (20). Briefly, 4 μm -thick FFPE tumor sections were stained using an automated staining system (Leica Microsystems, Buffalo Grove, IL) and two mIF panels with the following antibodies: Panel 1, cytokeratin (CK), CD3, CD8, PD-1/PD-L1, and CD68 and Panel 2, CK, CD3, CD8, CD45RO, granzyme B (GZB), and FOXP3. Antibody clones, dilutions and RRIDs are included in **Supplementary Table 2** and have been previously described (20). All the markers were stained in sequence using their respective fluorophore contained in the Opal 7-Color Automation IHC Kit (catalog # NEL821001KT; Akoya Biosciences, Waltham, MA). The slides were scanned using the Vectra/Polaris 3.0.3 (Akoya Biosciences) at low magnification, 10 \times (1.0 μm /pixel) through the full emission spectrum and positive tonsil controls from the run staining to calibrate the spectral image scanner protocol (21). A pathologist selected representative areas inside the tumor using regions of interest for scanning in high magnification by the Phenochart Software image viewer 1.0.12 (931 \times 698 μm size at resolution 20 \times = 0.5 μm /pixel) to capture various elements of tissue heterogeneity. Marker co-expression was employed to identify malignant cells (CK+), malignant cells expressing PD-L1 (CK+PD-L1+), and the cellular subsets of tumor-associated immune cells (TAICs) listed in **Supplementary Table 3**. Densities of each cell phenotype were quantified as the number of cells/ mm^2 in the tumor compartment characterized by group or nests of malignant cells, in the stroma compartment characterized by the fibrous tissue present between the tumor nets, and in both compartments described as a total. PD-L1+ malignant cells were also expressed in percentages. The data were consolidated using R studio 3.5.3 (Phenopter 0.2.2 packet; Akoya Biosciences).

Spatial point pattern distribution analysis

Using the point pattern distribution of the cell phenotypes relative to malignant cells, we measured the distance from malignant cells (CK+) to TAICs included in each mIF panel using R studio 3.5.3 (Phenopter 0.2.2 packet). We applied the median nearest neighbor function from malignant cells (CK+) to different cell phenotypes to determine where these TAICs were

located; specifically, whether the TAICs were close to (i.e., equal to or less than the median distance) or far from (i.e., more than the median distance) the malignant cells (CK+) and associated with clinical outcomes.

Spatial organization of cells by type

Cells were subset by phenotype using the markers in the mIF panels and examined as the following: Tumor/PD-L1+ (CK+PD-L1+), Tumor (CK+), Other-Tcells (CD3+), Other-Tcells/PD-1+ (CD3+PD-1+), Macrophages(CD68+), Macrophages/PD-L1+(CD68+PD-L1+), CTLs(CD3+CD8+) , CTLs/PD-1+(CD3+CD8+PD-1+), CTLs/GB+(CD3+CD8+GB+) and Tregs(CD3+CD8-Foxp3+). The above phenotypes were used to visualize the spatial organization of cells by type. This analysis was carried out in R version 4.2.0 (R studio 2022.07.2).

Spatial neighborhood

Using the marked planar point pattern representations of each mIF image, we calculated the spatially varying probabilities for each of the phenotypes (described above). We used the spatstat toolbox (22) which provides the relrisk function to identify areas of segregation for a multitype (markers >2) marked point pattern. This function estimates for each phenotype, the spatially varying probability or the ratios of the probabilities, using kernel smoothing. The output of this function was used to plot the contour of the spatially segregated neighborhoods for each phenotype.

Identifying cell clusters in the local neighborhood

We identified cell clusters in each image using Euclidean distance and a hierarchical clustering method. A minimum cluster size of 10 cells and distance ≤ 20 microns was the requirement for clustering. The distance based hierarchical clustering yielded the neighborhood information in a matrix. The cells that did not form clusters were labelled "Free_cell". The relative percentages of cells in each phenotype within a cluster was used to generate the heatmap. We used the SPIAT library (SPIAT version 1.0.4) to identify cell clusters and made additions to the SPIAT functions as required for our analysis using R version 4.2.0.

NanoString gene expression profiling

DNA and RNA were co-extracted from FFPE specimens received from the SWOG bank (**Supplementary Table 1**) and subjected to whole exome sequencing and gene expression. The RNA from a total of 38 FFPE samples (nivo = 23 and nivo+ipi = 15) passed the quality control

and was run on the nCounter platform using the PanCancer Immune Profiling Panel (730 immune-related and 40 housekeeping genes) per the manufacturer's instructions. Briefly, samples were hybridized overnight at 65°C to probes, excess probes were washed using the automated prep station and then imaged on the digital analyzer. All runs included a Human Reference RNA control for batch correction. Data were processed and normalized with NanoString's nSolver analysis software (23). All samples passed the post-run QC metrics, and no batch effects were evident in the runs. In addition, gene expression profiles were deconvoluted by TIMER and nSolver advanced analysis tools to infer immune cells correlated to clinical outcomes.

Whole-exome sequencing data analysis

WES analysis was conducted using the CIDC WES pipeline on tumor DNA from 50 tumors (nivo = 28 and nivo+ipi = 22, **Supplementary Table 1**) that passed the quality control. DNA from paired peripheral blood mononuclear samples was used as germ line control. WES implements Gene Analysis Toolkit (24) best practices and identifies somatic variants using Sentieon TNScope and Haplotyper algorithms (25), respectively. Somatic variants are annotated using the Variant Effect Predictor software (26). The pipeline uses an ensemble of three callers, CNVkit (27), Sequenza (28), and Facets (29), to characterize tumor copy number variation (CNV), and the CNV segments called by at least two callers were used to generate a high-confident consensus set. Sequenza and FACETS were used to estimate tumor purity and also PyClone-VI was utilized to infer clonal status of mutations (30). PyClone v 0.13.1 (31) was used to perform mutation clonality analysis. It is a Bayesian clustering method that enables mutations to be grouped into putative clonal clusters by integrating copy number, tumor purity (obtained from Sequenza), and variant allele frequency data.

Olink serum soluble analyte assay

We performed circulating serum analyte measurements using proximity extension assay (Olink) in 561 serum samples collected longitudinally from 160 patients (**Supplementary Table 1**). A series of 92 proteins, such as cytokines and soluble immune checkpoints included in the “immuno-oncology” panel, were measured as previously described (32). Protein levels were

normalized using internal positive and negative controls and quantified as log₂ protein expressions (NPX), which were subsequently used as input for downstream analysis.

Correlative analysis and statistical methods

To evaluate if the baseline biomarkers are prognostically associated with survival, we dichotomized biomarker data by the median and performed univariate survival analysis with the log-rank test. OS and PFS were evaluated. The Cox proportional hazard regression model was used for multivariate survival analysis (R package Survival, <https://CRAN.R-project.org/package=survival>) (33). We included TMB (≥ 10 or < 10 mutations per Mb), PD-L1 (≥ 5 or < 5 %), and other statistically significant biomarkers identified from univariate analysis in Cox models. Thresholds for TMB and PD-L1 were determined from previous clinical studies (18). To assess if continuous biomarker data are associated with response and other clinical variables, we used nonparametric tests: Spearman's rank correlation for continuous clinical variables, Mann-Whitney U test for categorical clinical variables with two groups, and Kruskal-Wallis test for categorical variables with more than two groups. In parallel, we also dichotomized biomarker data and used the chi-square test for a robust assessment with responders. The Benjamini-Hochbert (BH) method (34) was used for multiple-testing adjustment of P values. The analysis was performed on all samples and on samples in two treatment arms separately.

To explore the association of each baseline protein level with clinical outcomes from the Olink data, we used logistic regression models for best objective response and Cox proportional hazard models for PFS and OS (R package Survival, <https://CRAN.R-project.org/package=survival>, RRID: SCR_021137) (33). In separate regression models, univariate analyses included only the protein expression values, while the multiple variable analyses adjusted for additional covariates (i.e., treatment, age, sex, race, smoking). Then, to investigate the longitudinal changes in serum protein associated with treatment, we used mixed linear models (R package Dream and lme4) (35,36) and the timepoints baseline, cycle 2 week 3, cycle 4 week 7, and cycle 5 week 9 to quantify the effect of these variables and additional relevant clinical parameters. These were analyzed with the treatment arms nivo+ipi and nivo. In our models, each protein NPX was considered an independent variable. In contrast, phase, timepoints, and treatments were considered dependent variables and other covariates as random effects. This approach allowed us to quantify the variance across proteins and approximate

degrees of freedom of the hypothesis test for each protein, thereby minimizing false-positive results. We used F-tests for multiple coefficient comparisons and moderate t-tests for single coefficient comparisons.

To identify the differences between responders and nonresponders at each timepoint and longitudinally, we used time as a dependent variable. We jointly modeled survival with cytokine expression (R packages lme4, rstanarm: Bayesian applied regression modeling via Stan (RRID:SCR_024605), bayestestR, bayesplot: Plotting for Bayesian Models (<https://mc-stan.org/bayesplot/>, RRID: SCR_024588) (36,37) to investigate the association of longitudinal protein levels with survival outcomes. The model used Cox proportional hazards and linear mixed regression and assessed the association of dynamic biomarker changes with survival outcomes. In the random intercept, the independent variable was the number of months from baseline to biomarker collection, set as a natural spline with three knots (at most three changing time points between baseline and progression/death). The dependent variable was the Olink analyte NPX value. In the survival analysis component, the independent variable includes the treatment arms. The convergence of the Markov Chain Monte Carlo samples was assessed using several diagnostics: potential scale reduction factor, autocorrelation and trace plots, adequate sample size, and Monte Carlo Standard Error (32,38-40). Finally, we used the false discovery rate (FDR) as the preferred method to correct for multiple hypothesis testing. The thresholds for significance in the mixed linear models for differential expression tests were a \log_2 fold change of at least 0.5 and an $FDR < 0.05$. The joint model's threshold for significance was at least 1 unit increase in \log_2 NPX expression and $FDR < 0.05$.

For integrative analysis, we applied recursive partitioning tree analysis (RPART, rpart library in R, <https://cran.r-project.org/web/packages/rpart/vignettes/longintro.pdf>) and random forest (41,42) (RF, randomForest and randomForestSRC libraries in R) on Olink (N=159) and mIF (N=82) data. We fitted RPART tree using responder status as the dependent variable, 92 baseline level Olink proteins and 17 mIF markers as predictors. We also created decision tree survival prediction model. Separate RPART trees were fitted for mIF markers from different compartments along with Olink proteins. The minimum number of observations in a node for a split was set to be 15; 10-fold cross-validation was carried out and results used for tree-pruning. For RF, we used 81 samples with both Olink and mIF data. Bootstrap the data to create bootstrap samples; grow a survival tree for each bootstrap sample with split criteria based on the log-rank

statistics; continue the recursive partition; and calculate importance of each predictor by averaging over the forest.

Data Availability

In conjunction with the clinical study principal investigator/chair, the NCI-sponsored network and CIDC, we will make available de-identified data publicly available by request under the dbGaP PHS accession number: phs003412.v1.p1. Questions and requests for additional data can be directed to the corresponding author.

Results

Clinical characteristics

There were 31 responders (19.4%), including complete responses, partial responses, and unconfirmed partial/complete response; 63 patients with stable disease (39.4%); and 61 patients (38.1%) with progressive disease (i.e., increasing disease and symptomatic deterioration). Overall, 31 patients (19.4%) were alive at the end of the study, and the median OS was 10.02 months (range 0.3–40.3). One hundred and forty-eight patients (92.5%) had disease progression, with a median PFS of 3.4 months (range 0.3–36.6, **Supplementary Table 1**).

An active immune infiltration is associated with benefit from ICI treatment

We first analyzed the mIF and gene expression profiling data from baseline tissue samples taken before ICI treatment to identify immune features associated with clinical benefit. mIF data revealed higher densities of various immune cells in the stroma compartment compared to the tumor compartment across the whole cohort (nivo+ipi and nivo arms), with no significant differences between the nivo+ipi and nivo arms (**Supplementary Table 4**). The overall immune cell densities were higher in the responders across both arms, although the difference did not reach statistical significance. In the whole cohort, higher median densities of PD-1+ cytotoxic T cells (CTLs; CD3+CD8+PD-1+) in the stroma (>4.1 cells/mm², $P = 0.042$), presence of GZB+ CTLs in the tumor compartment (>0 cells/mm², $P = 0.011$), and higher median densities of memory T cells (CD3+CD45RO+; >23.4 cells/mm², $P = 0.041$) and PD-1+ T cells (CD3+PD-1+; >16.0 cells/mm², $P = 0.023$) in the total compartment (tumor plus stroma) were associated with longer PFS (**Supplementary Table 5**). Similarly, transcriptomic analysis demonstrated that

patients having tumors with a higher expression of genes associated with myeloid infiltration, immune recruitment, and inflammation had superior clinical outcomes in the whole cohort (**Table 1** and **Supplementary Table 6**). The associations between higher expression of CD163, BLNK, IRF1, FCGR2A with better OS ($P < 0.05$) and higher expression of MAPK11 with worse OS remained significant in subsequent multivariate analyses after adjustments for known predictive biomarkers, including TMB and PD-L1.

In the nivo arm, higher densities of memory T cells (CD3+CD45RO+) in the total compartment (median > 24.6 cells/mm², $P = 0.028$) and memory/regulatory T cells (CD3+CD8-CD45RO+FOXP3+) in the total compartment (median > 4.6 cells/mm², $P < 0.001$) and the stroma compartment (median > 12.0 cells/mm², $P = 0.049$) were associated with longer PFS (**Table 2** and **Figure 1A and 1B**). Higher densities of memory/regulatory T cells (CD3+CD8-CD45RO+FOXP3+) in the total compartment (median > 4.6 cells/mm², $P = 0.026$) were associated with better OS (**Table 2** and **Figure 1C**). In the nivo+ipi arm, higher densities of PD-1+ T cells (CD3+PD-1+) in the total compartment (median > 16.0 cells/mm², $P = 0.0347$) and the presence of GZM+ CTLs (CD3+CD8+GZB+) in the tumor compartment (>0 cells/mm², $P = 0.0154$) were associated with longer PFS (**Table 2** and **Figure 1D and E**). Conversely, higher densities of regulatory T cells (Tregs; CD3+CD8-FOXP3+) in the total compartment (median > 12.4 cells/mm², $P = 0.0418$) were associated with worse OS (**Table 2** and **Figure 1F**). In the nivo+ipi arm, deconvolution of transcriptomic profiling data by TIMER and nSolver demonstrated significantly higher total immune cells (CD45+), a higher exhausted CD8+ T-cell score, and a higher neutrophil score in responders vs. nonresponders ($P < 0.05$, **Figure 1G to 1I**), further supporting that overall higher immune infiltration is associated with superior clinical benefit from ICI treatment.

High infiltration of cytotoxic T cells is associated with exceptional response to ICIs

Next, we specifically investigated exceptional responders, defined as patients who had no progression for at least 18 months and were still alive by 24 months, vs. early progressors, who survived more than 1 month but had progressive disease and died within 6 months after initiating ICI treatment. By these definitions, there were 11 exceptional responders and 44 early progressors across the total trial cohort (**Figure 2A**). There were more exceptional responders in the nivo+ipi arm than in the nivo arm (7 of 73 vs. 4 of 87, $P = 0.35$). Among these patients, 8

exceptional responders and 21 early progressors had tissues available for mIF, and 6 exceptional responders and 8 early progressors had tissues available for gene expression analysis.

By mIF, we observed higher densities of CTLs (CD3+CD8+) and memory CTLs (CD3+CD8+CD45RO+) in the total compartment in exceptional responders than in early progressors (CTLs: median, 152.1 vs. 27.3 cells/mm²; $P = 0.032$; memory CTLs: median, 31.2 vs. 2.1 cells/mm²; $P = 0.040$; **Supplementary Table 7**). Representative images from an exceptional responder are shown in **Figure 2B and 2C**. Moreover, in the tumor compartment, we observed higher densities of GZB+ CTLs (CD3+CD8+GZB+) in the exceptional responders than the early progressors (median, 3.6 vs. 0 cells/mm², $P = 0.027$) (**Figure 2D**). Representative images from an early progressor showing a lower density of immune infiltration are shown in **Figure 2E and 2F**.

Furthermore, distinctive spatial neighborhoods and cell organization in TME were observed in exceptional responders (n=6) relative to early progressors (n=6) (**Figure 2 (G-J) and Supplementary Figures 2 and 3**). Shown in **Figure 2G, Supplementary Figures 2A and 3A** is the distribution of different cell subsets relative to each other, with higher immune infiltration and higher CTL densities in the TME of exceptional responders vs. early progressors. We then used spatially varying probabilities of different cell phenotypes to determine the segregation among immune subsets and malignant cells, and a contour plot to represent the neighborhoods within the TMEs. These analyses revealed a higher spatial segregation of immune cell subsets relative to malignant cells in the early progressors as compared to the exceptional responders (**Figure 2H, Supplementary Figures 2B and 3B**) in line with above observation that higher densities of CTLs in the tumor region positively associated with survival. Through distance-based hierarchical clustering, we identified local cell clusters within the TME and observed distinct compositions in exceptional responders vs. early progressors. The clusters (cells ≥ 10 within interacting distance 20 microns) in exceptional responders often consisted of CTLs and other-T cell populations in the proximity to tumor cells (**Figure 2 I-J, Supplementary Figures 2C-D, 3C-D**). Finally, infiltration of neutrophils inferred from gene expression profiling data was significantly higher in exceptional responders than early progressors ($P = 0.029$; **Supplementary Figure 4**).

Close proximity of T cells and malignant cells is associated with benefit from ICIs

Given the recognized importance of distance between different cells and the clustering of CTLs and tumor cells observed in exceptional responders, we expanded our analysis to understand the spatial relationship between the cell types associated with clinical outcome described above with other cells within the tumor microenvironment (43,44). In the whole cohort, shorter distances from malignant cells (CK+) as well as PD-L1+ malignant cells (CK+PD-L1+) to CTLs (CD3+CD8+; median, 139 μ m and 148 μ m) were associated with better PFS ($P = 0.045$ and $P = 0.027$, respectively); and shorter distances from malignant cells (CK+) to GZB+ CTLs (CD3+CD8+GZB+) were associated with significantly longer PFS ($P = 0.035$) and a trend toward longer OS ($P = 0.054$; **Figure 3A to 3E**). In the nivo+ipi arm, shorter distances of CTLs (CD3+CD8+) as well as GZB+ CTLs (CD3+CD8+GZB+) from malignant cells (CK+; $P = 0.045$ and, $P = 0.026$, respectively) and shorter distances between CTLs (CD3+CD8+) from PD-L1+ malignant cells (CK+PD-L1+; $P = 0.033$) were associated with longer PFS (**Figure 3F,3G and 3H**). In addition, shorter distances of GZB+ CTLs (CD3+CD8+GZB+; median, 245 μ m) from malignant cells (CK+) were associated with longer OS ($P = 0.045$; **Figure 3I**). Taken together, these results suggest that the immune cells' density and spatial distribution may impact response to ICI therapy.

High CNV burden is associated with cold immune infiltration

We next performed WES ($n = 50$) with the intent of identifying the genomic basis underlying the immune features associated with benefit from nivo+ipi vs. nivo in these metastatic squamous cell carcinomas. A total of 30,081 non-silent mutations were detected with transversions, particularly C>A, as the predominant substitutes, which was expected because most patients were smokers (**Supplementary Figure 5A**). The commonly mutated cancer genes included *TP53*, *LRP1B*, *CDKN2A*, *ARID1A*, and *PIK3CA* (**Supplementary Figure 5B**). High CNV burden was associated with a colder tumor immune microenvironment, as evidenced by lower infiltration levels of overall CD3+ T cells from mIF and lower levels of various immune signatures derived from gene expression profiling (**Supplementary Figure 6A and 6B**). Importantly, CNV burden was not associated with estimated tumor purity, suggesting the correlation between high CNV burden and cold tumor immune microenvironment was not due to relative high tumor cell density leading to dilution of immune cells. Taken together, these results indicate that chromosomal instability may be an underlying genomic feature associated with

immune evasion in metastatic SqNSCLC. Among the commonly mutated cancer genes, mutations in *LRP1B*, a recently recognized potential regulator of the inflammatory response, was associated with less infiltration of GZB+ CTLs (CD3+CD8+GZB+; **Supplementary Figure 7A**) (45,46). Interestingly, *LRP1B* mutations were enriched in nonresponders but not in responders (18/19 vs. 2/11, $P = 0.049$). Furthermore, patients with *LRP1B* mutations had significantly ($P = 0.008$) shorter PFS (**Supplementary Figure 7B**) and numerically shorter OS in the overall cohort (**Supplementary Figure 7C**). *LRP1B*-mutant tumors were not associated with short PFS in the nivo+ipi arm (**Supplementary Figure 7D**) but were in the nivo arm ($P = 0.033$; **Supplementary Figure 7E**).

Dynamic changes in peripheral blood cytokines are associated with benefit from ICIs

Blood-based biomarkers are attractive because they are noninvasive, dynamic, and less impacted by intra-tumor heterogeneity than tissue-based markers (47). We performed Olink proximity extension assay using the immuno-oncology panel assaying a series of 92 proteins in 561 serum samples collected longitudinally from 160 patients. Using mixed models to account for demographic and relevant clinical covariates with multiple testing adjustments, several serum chemokines (CXCL9, CXCL10, CXCL13, CCL19) and activated T-cell markers (PD-1, IFN- γ , IL-12, IL-10) were found durably increased from baseline with either nivo or nivo+ipi, (**Figure 4A and 4B**) indicating the ICIs' immune regulating effect. Multiple markers of immune activation and priming (ICOS-L, LAMP3/DC-LAMP, IL-4, IL-13, NRC1, CD5) were found increased at baseline or early during treatment in responders, regardless of treatment type ($P < 0.05$; **Figure 4C and 4D**), in line with associations of these important immune processes with clinical response to ICI. Conversely, macrophage-derived and hyperinflammation markers, such as IL-6, IL-8, CXCL13, CSF-1, TNFSF14/LIGHT, and CCL23, as well as likely stromal or tumor-derived markers, such as VEGFA, HGF, and HO-1, were significantly upregulated in nonresponders at baseline or after ICI preceding radiologic progression, with some differences based on treatment received for CXCL13 and CSF-1 ($P < 0.05$; **Figure 4C and 4D**). Joint modeling of survival with Olink analytes showed an increased risk of death ($HR > 1$) with higher longitudinal serum levels of CXCL13, MMP12, CSF-1, and IL-8, which was confirmed with independent Kaplan-Meier analyses based on median protein levels at baseline (**Figure 4E**). Similar results were generally observed in the subset of patients with extreme outcomes

(exceptional responders and early progressors), where LAMP3/DC-LAMP was higher while CXCL13, CCL23, and TNFSF14 were lower in exceptional responders at baseline compared to nonresponders (**Figure 4F**, $P < 0.05$). Together with the above-described data, and considering only baseline markers, these results suggest that an activated T cell signature (cytotoxic effector T cells and DC-LAMP) was important for responsiveness to treatment with either nivo or nivo+ipi, while a hyperinflammatory milieu (IL-6, IL-8, CXCL13, CCL23, TNFSF14/LIGHT, CSF-1, MMP12) had an adverse impact on response and OS.

Integrative analysis of immune features across different platforms

The anti-tumor immunity and response to ICIs is often determined at different molecular levels. The multiomics profiling in this study provided a unique opportunity for integrative analysis to understand the molecular and immune features associated with ICI benefit. We first performed recursive partitioning on Olink, mIF, Nanostring, and WES data for classification of responders (**Supplementary Figure 8A and B**). We identified that proteins from Olink provide good prediction on response. However, mIF markers did not contribute significantly in the decision tree, which might be due to relatively small sample size for mIF (n=159 for Olink and n=82 for mIF). We next created a decision tree survival prediction model and observed that Cytotoxic.T.cells.antigen.experienced (CD3+CD8+PD-1+) together with IL6, LAG3 and MICA.B separate patients into sub-populations with different survival. Furthermore, we applied random forest classifier, which identified Cytotoxic.T.cells.antigen.experienced (CD3+CD8+PD-1+) and IL6 as important variables. Nanostring and WES did not contribute to the association between omics markers and outcomes likely due to insufficient samples with data from these platforms.

Discussion

Identifying novel biomarkers for ICI response is challenging because the molecular determination of tumor microenvironment and host immune response is complex and heterogeneous across different patients. A large sample size to control inter-patient heterogeneity and multi-omics to identify the determinates at different molecular levels are ideal but challenging. Therefore, maximizing the use of clinical, pathological, molecular data and learning

from each patient, particularly from clinical trials and careful analysis is key to pave the way to advance our understanding and ultimately the efficacy of ICI.

In this study, we performed mIF, gene expression profiling, WES, and OLINK on the previous samples from S1400I and identified known and novel molecular features associated with nivo monotherapy vs. nivo+ipi combination. Responders demonstrated higher densities of multiple immune cell types defined by mIF. Analysis of CTL populations revealed that GZB+ CTLs (CD3+CD8+GZB+) located in the tumor compartment were associated with better PFS. This was corroborated by analyzing the spatial organization of cell phenotypes, whereas higher immune cell population in the tumor region was seen in the TME of exceptional responders than that of early progressors. On the other hand, higher densities of Tregs (CD3+CD8-FOXP3+) in the total compartment correlated with worse OS in the nivo+ipi arm. This highlights the emerging dichotomy regarding the impact of ICI therapies on Treg subsets and function (48), as these combinations may not modulate some Treg subsets and dominance of CTLs is needed to overcome local immune suppression. Conversely, higher densities of memory T cells (CD3+CD45RO+) and regulatory/memory T cells (CD3+CD8-CD45RO+FOXP3+) were associated with better PFS in the nivo monotherapy arm. As PD-1 targeting has been shown to result in the re-activation of T cells already present within the tumor immune microenvironment, the presence of regulatory/memory T cells at baseline may be an essential biomarker to delineate the need for inclusion of ipilimumab as opposed to a nivolumab alone approach. Estimating the immune subsets using TIMER and nSolver software demonstrated that a higher immune presence was associated with improved outcome. These results emphasize that an active immune response within the tumor microenvironment is required for a favorable clinical outcome in this setting, which is supported by multiple findings identifying mechanisms of response to ICI-based therapeutic strategies across various cancer types (49-51).

The tumor microenvironment is composed of various immune cells and stroma cells entangled with cancer cells. In addition to the densities of different cells, the spatial distribution and proximity among various cell types are also essential features with important impact on the functional status of the tumor immune microenvironment (52,53). mIF data from this study provided an opportunity to assess the spatial relationship of different cellular components within the tumor immune microenvironment and their association with clinical outcomes from ICI treatment. Using the spatial point metrics through the nearest neighbor analysis, we observed that

tumors with higher densities of GZB+ CTLs close to malignant cells were associated with better PFS and OS in the nivo+ipi arm, suggesting that cell-to-cell distribution and specially CTLs play an important role in response to ICIs as showed by others studies in NSCLC (54). The organization of cells into clusters based on distance also demonstrated that the CTLs and malignant cells cluster more frequently in exceptional responders than early progressors suggesting a pre-formed anti-tumor response that is aided by the ICI.

We used WES to identify genomic features underlying particular immune features and found that a higher CNV burden was associated with a lower level of immune cell infiltration overall. Similarly, CNV burden was negatively associated with immune scores derived from immune gene expression profiling. These findings are in line with previous findings in different cancer types suggesting that chromosomal instability may be a common genomic alteration underlying immune evasion across human malignancies (53,55-58). Interestingly, we also found that patients with *LRP1B*-mutant tumors had a reduced survival compared to patients without *LRP1B* mutations. *LRP1B* has been identified as a putative tumor suppressor and is frequently inactivated in NSCLCs (45). Recently, *LRP1B* mutation was reported to be associated with better prognosis in melanoma and NSCLC after anti-PD-1 therapy (46). However, in our cohort, we observed that *LRP1B* mutation was associated with a worse OS and PFS in both the nivo monotherapy arm and nivo+ipi combination therapy arms. It is still unclear whether the difference was due to different histology (predominantly adenocarcinoma in the previous study vs. exclusively squamous cell carcinoma in the current study) or different ICI (anti-PD-1 vs. anti-PD-1 with/without anti-CTLA-4) or low sample size. Of note, the impact of *LRP1B* mutations on cancer biology and response to ICIs has not been clearly defined in different cancers. For example, a study on renal clear-cell carcinoma reported worse prognosis and suppressive antitumor immunity when *LRP1B* was overexpressed (59), and another found that *LRP1B* mutations were associated with inferior clinical outcomes after ICI treatment in hepatocellular carcinoma patients (60).

Although tissue-based assays remain the gold standard for molecular profiling for oncology practice, liquid biopsy, particularly peripheral blood-based assays, have gained more attention for molecular profiling and disease monitoring across various cancers because they are noninvasive, “real-time,” and less affected by intra-tumor heterogeneity (61,62). In the era of immune-oncology, the Olink soluble protein detection platform has emerged as a promising tool

to assess and monitor host immune response. Using Olink, we identified a high level of pro-tumorigenic factors, such as VEGFA and CCL23, and inflammatory markers, such as IL-6, IL-8, and MMP-12, that were associated with inferior survival in this cohort of patients. These findings suggest that general inflammation is detrimental in the context of cancer and ICI therapy. In contrast, proteins involved in T-cell and NK activation, such as LAMP3/DC-LAMP, IFN- γ /IL-4/IL-13, and NRC-1, were associated with improved outcomes after ICI therapy. It was unexpected that a high level of CXCL13 was associated with poor response to ICI therapy and shorter survival, given the recent studies reporting this chemokine working together with DC-LAMP and playing essential roles in the establishment of tertiary lymphoid structures in NSCLC (63). It is possible that the relatively high levels of circulating CXCL13 in the serum do not reflect relatively rare CD4+ T cell–derived tumor tissue–specific expression of CXCL13, and this emphasizes the limitations of soluble analytes as a surrogate for local tumor events. Some analytes, such as CXCL9/10 and soluble PD-1, were dynamically increased with treatment and marginally associated with outcomes in exceptional responders, in line with previous reports (64). Of particular interest, other markers showed the strongest association with objective response during ICI treatment, e.g., lower CSF-1 or IL-6 or higher IL-13 at cycle 2. This is reminiscent of findings from melanoma studies in which the on-treatment biopsy was more informative for long-term benefit from ICIs than the baseline biopsy, as the actual changes after treatment reflect the host immune system’s response to ICIs more accurately (65,66). Although soluble analytes are not ideal predictive biomarkers to select an optimal initial treatment regimen, if validated, these markers will be extremely helpful in switching ineffective therapy to effective alternatives to save time and potential toxicity, which is critically important for patients with stage IV lung cancers, for whom time and quality of life are essential attributes. Additionally, these on-treatment markers are also valuable in distinguishing pseudoprogression from real progression—another critical clinical dilemma that the oncologists face in the era of immuno-oncology.

As a post-hoc profiling of samples from a completed clinical trial, our study has several inherent limitations, including inadequate tumor specimen availability, which precluded us from generating comprehensive data integration from all platforms; imbalanced distribution of samples from the nivo vs. nivo+ipi arms or responders vs. nonresponders; inadequate tissues for multiomic analysis and cross-platform integrative analyses; and lack of detailed information

regarding the time and anatomic sites of tumor specimens, which limited our ability to perform in-depth, organ-specific analysis. In spite of these challenges, integration of peripheral cytokine profiling and cellular profiling within the TME confirmed our single platform findings highlighting the negative association with hyper-inflammation with reduced PFS and the presence of PD-1+ CTLs in the TME with increased survival. Finally, while we presented several candidates in this study, we recognize the need for additional validation and replication of our findings. Specifically, several circulating serum proteins, such as IL-6-8, CSF1, MMP12, and CXCL13 are promising candidates for future prospective or post-hoc confirmatory studies due to their ease of collection and quantification from blood. In addition, investigation of tissue composition using spatial profiling technologies to better understand the complex interplay between tumor tissue and immune infiltrating cells may shed light on the mechanisms of immune-tumor cell-cell interactions and identify key biomarkers that can identify patients who will have the most benefit from ICIs. As a proof-of-principle study, using the S1400I trial as an example, we showcased that multi-omics, multi-institutional analyses of patient samples are feasible and can provide valuable insights for future trial development, which is one of the major goals of the CIMAC-CIDC Network.

Acknowledgments

Scientific and financial support for the CIMAC-CIDC Network is provided through the National Cancer Institute (NCI) Cooperative Agreements U24CA224319 (to the Icahn School of Medicine at Mount Sinai CIMAC), U24CA224285 (to MD Anderson Cancer Center CIMAC) and U24CA224316 (to the CIDC at Dana-Farber Cancer Institute). SWOG Study S1400I was supported in part by NIH/NCI grants U10CA180888 and U10CA180819 and in part by Bristol-Myers Squibb Company, through the Foundation for the National Institutes of Health, in partnership with Friends of Cancer Research. Scientific and financial support for the Partnership for Accelerating Cancer Therapies (PACT) public-private partnership (PPP) are made possible through funding support provided to the FNIH by: AbbVie Inc., Amgen Inc., Boehringer-Ingelheim Pharma GmbH & Co. KG., Bristol-Myers Squibb, Celgene Corporation, Genentech Inc, Gilead, GlaxoSmithKline plc, Janssen Pharmaceutical Companies of Johnson & Johnson, Novartis Institutes for Biomedical Research, Pfizer Inc., and Sanofi.

We thank the members of the Translational Molecular Pathology Immune-Profiling (TMP-IL) MoonShots Platform at MD Anderson for their support. We thank Beatriz Sanchez-Espiridion, Julia Mendoza Perez, Shani Wijeratne, and Celia Garcia-Prieto for their assistance with sample procurement and inventory; Mei Jiang, Auriole Tamegnon, Heladio Ibarguen, Salome McAllen, Saxon Rodriguez, Jianling Zhou, Mauricio E Vasquez Juarez, and Renganayaki Krishna Pandurengan for their technical assistance; Dawen Sui and Juan Ruiz Posadas for data transfer; and Curtis Gumbs and Latasha Little for genomics support. Seunghee Kim-Schulze, for his help in running Olink assays. We thank Diane Del Valle for project management from the Mt. Sinai CIMAC, Magdalena Thurin, Helen Chen, Minkyung Song from NCI and Rebecca Enos from Emmes. Editorial support was provided by Bryan Tutt, Scientific Editor, Research Medical Library at MD Anderson Cancer Center We thank the patients and their families for participating in the study.

References

1. Topalian SL, Hodi FS, Brahmer JR, Gettinger SN, Smith DC, McDermott DF, *et al.* Safety, activity, and immune correlates of anti-PD-1 antibody in cancer. *N Engl J Med* 2012;**366**(26):2443-54 doi 10.1056/NEJMoa1200690.
2. Brahmer J, Reckamp KL, Baas P, Crino L, Eberhardt WE, Poddubskaya E, *et al.* Nivolumab versus Docetaxel in Advanced Squamous-Cell Non-Small-Cell Lung Cancer. *N Engl J Med* 2015;**373**(2):123-35 doi 10.1056/NEJMoa1504627.
3. Herbst RS, Baas P, Kim DW, Felip E, Perez-Gracia JL, Han JY, *et al.* Pembrolizumab versus docetaxel for previously treated, PD-L1-positive, advanced non-small-cell lung cancer (KEYNOTE-010): a randomised controlled trial. *Lancet* 2016;**387**(10027):1540-50 doi 10.1016/S0140-6736(15)01281-7.
4. Fehrenbacher L, von Pawel J, Park K, Rittmeyer A, Gandara DR, Ponce Aix S, *et al.* Updated Efficacy Analysis Including Secondary Population Results for OAK: A Randomized Phase III Study of Atezolizumab versus Docetaxel in Patients with Previously Treated Advanced Non-Small Cell Lung Cancer. *J Thorac Oncol* 2018;**13**(8):1156-70 doi 10.1016/j.jtho.2018.04.039.
5. Paz-Ares L, Luft A, Vicente D, Tafreshi A, Gumus M, Mazieres J, *et al.* Pembrolizumab plus Chemotherapy for Squamous Non-Small-Cell Lung Cancer. *N Engl J Med* 2018;**379**(21):2040-51 doi 10.1056/NEJMoa1810865.
6. West H, McCleod M, Hussein M, Morabito A, Rittmeyer A, Conter HJ, *et al.* Atezolizumab in combination with carboplatin plus nab-paclitaxel chemotherapy compared with chemotherapy alone as first-line treatment for metastatic non-squamous non-small-cell lung cancer (IMpower130): a multicentre, randomised, open-label, phase 3 trial. *Lancet Oncol* 2019;**20**(7):924-37 doi 10.1016/S1470-2045(19)30167-6.
7. Hellmann MD, Paz-Ares L, Bernabe Caro R, Zurawski B, Kim SW, Carcereny Costa E, *et al.* Nivolumab plus Ipilimumab in Advanced Non-Small-Cell Lung Cancer. *N Engl J Med* 2019;**381**(21):2020-31 doi 10.1056/NEJMoa1910231.
8. Paz-Ares L, Ciuleanu TE, Cobo M, Schenker M, Zurawski B, Menezes J, *et al.* First-line nivolumab plus ipilimumab combined with two cycles of chemotherapy in patients with non-small-cell lung cancer (CheckMate 9LA): an international, randomised, open-label, phase 3 trial. *Lancet Oncol* 2021;**22**(2):198-211 doi 10.1016/S1470-2045(20)30641-0.
9. Li F, Dong X. Pembrolizumab provides long-term survival benefits in advanced non-small cell lung cancer: The 5-year outcomes of the KEYNOTE-024 trial. *Thorac Cancer* 2021;**12**(23):3085-7 doi 10.1111/1759-7714.14193.
10. Jassem J, de Marinis F, Giaccone G, Vergnenegre A, Barrios CH, Morise M, *et al.* Updated Overall Survival Analysis From IMpower110: Atezolizumab Versus Platinum-Based Chemotherapy in Treatment-Naive Programmed Death-Ligand 1-Selected NSCLC. *J Thorac Oncol* 2021;**16**(11):1872-82 doi 10.1016/j.jtho.2021.06.019.
11. Neoadjuvant PD-1 Blockade in Resectable Lung Cancer; Nivolumab and Ipilimumab in Advanced Melanoma; Overall Survival with Combined Nivolumab and Ipilimumab in Advanced Melanoma; Prolonged Survival in Stage III Melanoma with Ipilimumab Adjuvant Therapy; Combined Nivolumab and Ipilimumab or Monotherapy in Untreated Melanoma; Combined Nivolumab and Ipilimumab or Monotherapy in Untreated Melanoma; Nivolumab and Ipilimumab versus Ipilimumab in Untreated Melanoma; Rapid Eradication of a Bulky Melanoma Mass with One Dose of Immunotherapy; Genetic Basis for Clinical Response to CTLA-4 Blockade; Genetic Basis for Clinical Response to CTLA-4 Blockade in Melanoma; Nivolumab plus Ipilimumab in Advanced Melanoma; Safety and Tumor Responses with Lambrolizumab (Anti-PD-1) in Melanoma; Hepatotoxicity with Combination of Vemurafenib and Ipilimumab. *N Engl J Med* 2018;**379**(22):2185 doi 10.1056/NEJMx180040.

12. Wolchok JD, Chiarion-Sileni V, Gonzalez R, Rutkowski P, Grob JJ, Cowey CL, *et al.* Overall Survival with Combined Nivolumab and Ipilimumab in Advanced Melanoma. *N Engl J Med* 2017;**377**(14):1345-56 doi 10.1056/NEJMoa1709684.
13. Ready N, Hellmann MD, Awad MM, Otterson GA, Gutierrez M, Gainor JF, *et al.* First-Line Nivolumab Plus Ipilimumab in Advanced Non-Small-Cell Lung Cancer (CheckMate 568): Outcomes by Programmed Death Ligand 1 and Tumor Mutational Burden as Biomarkers. *J Clin Oncol* 2019;**37**(12):992-1000 doi 10.1200/JCO.18.01042.
14. Hellmann MD, Rizvi NA, Goldman JW, Gettinger SN, Borghaei H, Brahmer JR, *et al.* Nivolumab plus ipilimumab as first-line treatment for advanced non-small-cell lung cancer (CheckMate 012): results of an open-label, phase 1, multicohort study. *Lancet Oncol* 2017;**18**(1):31-41 doi 10.1016/S1470-2045(16)30624-6.
15. Gettinger SN, Redman MW, Bazhenova L, Hirsch FR, Mack PC, Schwartz LH, *et al.* Nivolumab Plus Ipilimumab vs Nivolumab for Previously Treated Patients With Stage IV Squamous Cell Lung Cancer: The Lung-MAP S1400I Phase 3 Randomized Clinical Trial. *JAMA Oncol* 2021;**7**(9):1368-77 doi 10.1001/jamaoncol.2021.2209.
16. Hong L, Negrao MV, Dibaj SS, Chen R, Reuben A, Bohac JM, *et al.* Programmed Death-Ligand 1 Heterogeneity and Its Impact on Benefit From Immune Checkpoint Inhibitors in NSCLC. *J Thorac Oncol* 2020;**15**(9):1449-59 doi 10.1016/j.jtho.2020.04.026.
17. Herbst RS, Soria JC, Kowanetz M, Fine GD, Hamid O, Gordon MS, *et al.* Predictive correlates of response to the anti-PD-L1 antibody MPDL3280A in cancer patients. *Nature* 2014;**515**(7528):563-7 doi 10.1038/nature14011.
18. Klempner SJ, Fabrizio D, Bane S, Reinhart M, Peoples T, Ali SM, *et al.* Tumor Mutational Burden as a Predictive Biomarker for Response to Immune Checkpoint Inhibitors: A Review of Current Evidence. *Oncologist* 2020;**25**(1):e147-e59 doi 10.1634/theoncologist.2019-0244.
19. Hellmann MD, Nathanson T, Rizvi H, Creelan BC, Sanchez-Vega F, Ahuja A, *et al.* Genomic Features of Response to Combination Immunotherapy in Patients with Advanced Non-Small-Cell Lung Cancer. *Cancer Cell* 2018;**33**(5):843-52 e4 doi 10.1016/j.ccell.2018.03.018.
20. Parra ER, Ferrufino-Schmidt MC, Tamegnon A, Zhang J, Solis L, Jiang M, *et al.* Immuno-profiling and cellular spatial analysis using five immune oncology multiplex immunofluorescence panels for paraffin tumor tissue. *Sci Rep* 2021;**11**(1):8511 doi 10.1038/s41598-021-88156-0.
21. Parra ER, Jiang M, Solis L, Mino B, Laberiano C, Hernandez S, *et al.* Procedural Requirements and Recommendations for Multiplex Immunofluorescence Tyramide Signal Amplification Assays to Support Translational Oncology Studies. *Cancers (Basel)* 2020;**12**(2) doi 10.3390/cancers12020255.
22. Baddeley A, Turner R. spatstat: An R Package for Analyzing Spatial Point Patterns. *Journal of Statistical Software* 2005;**12**(6):1 - 42 doi 10.18637/jss.v012.i06.
23. Waggott D, Chu K, Yin S, Wouters BG, Liu FF, Boutros PC. NanoStringNorm: an extensible R package for the pre-processing of NanoString mRNA and miRNA data. *Bioinformatics* 2012;**28**(11):1546-8 doi 10.1093/bioinformatics/bts188.
24. McKenna A, Hanna M, Banks E, Sivachenko A, Cibulskis K, Kernytsky A, *et al.* The Genome Analysis Toolkit: a MapReduce framework for analyzing next-generation DNA sequencing data. *Genome Res* 2010;**20**(9):1297-303 doi 10.1101/gr.107524.110.
25. Kendig KI, Baheti S, Bockol MA, Drucker TM, Hart SN, Heldenbrand JR, *et al.* Sentieon DNaseq Variant Calling Workflow Demonstrates Strong Computational Performance and Accuracy. *Front Genet* 2019;**10**:736 doi 10.3389/fgene.2019.00736.
26. McLaren W, Gil L, Hunt SE, Riat HS, Ritchie GR, Thormann A, *et al.* The Ensembl Variant Effect Predictor. *Genome Biol* 2016;**17**(1):122 doi 10.1186/s13059-016-0974-4.
27. Talevich E, Shain AH, Botton T, Bastian BC. CNVkit: Genome-Wide Copy Number Detection and Visualization from Targeted DNA Sequencing. *PLoS Comput Biol* 2016;**12**(4):e1004873 doi 10.1371/journal.pcbi.1004873.

28. Favero F, Joshi T, Marquard AM, Birkbak NJ, Krzystanek M, Li Q, *et al.* Sequenza: allele-specific copy number and mutation profiles from tumor sequencing data. *Ann Oncol* 2015;**26**(1):64-70 doi 10.1093/annonc/mdu479.
29. Shen R, Seshan VE. FACETS: allele-specific copy number and clonal heterogeneity analysis tool for high-throughput DNA sequencing. *Nucleic Acids Res* 2016;**44**(16):e131 doi 10.1093/nar/gkw520.
30. Gillis S, Roth A. PyClone-VI: scalable inference of clonal population structures using whole genome data. *BMC Bioinformatics* 2020;**21**(1):571 doi 10.1186/s12859-020-03919-2.
31. Roth A, Khattra J, Yap D, Wan A, Laks E, Biele J, *et al.* PyClone: statistical inference of clonal population structure in cancer. *Nat Methods* 2014;**11**(4):396-8 doi 10.1038/nmeth.2883.
32. Monjazebe AM, Giobbie-Hurder A, Lako A, Thrash EM, Brennick RC, Kao KZ, *et al.* Correction: A Randomized Trial of Combined PD-L1 and CTLA-4 Inhibition with Targeted Low-dose or Hypofractionated Radiation for Patients with Metastatic Colorectal Cancer. *Clin Cancer Res* 2021;**27**(17):4940 doi 10.1158/1078-0432.CCR-21-2698.
33. Therneau TM, Grambsch, P.M. . Modeling Survival Data: Extending the Cox Model. New York: Springer; 2000.
34. Benjamini Y, Cohen R. Weighted false discovery rate controlling procedures for clinical trials. *Biostatistics* 2017;**18**(1):91-104 doi 10.1093/biostatistics/kxw030.
35. Hoffman GE, Roussos P. Dream: powerful differential expression analysis for repeated measures designs. *Bioinformatics* 2021;**37**(2):192-201 doi 10.1093/bioinformatics/btaa687.
36. Bates D, Mächler, M., Bolker, B., Walker, S. . Fitting Linear Mixed-Effects Models Using lme4. *Journal of Statistical Software* 2015;**67**(1):1–48 doi doi: 10.18637/jss.v067.i01.
37. Makowski D, Ben-Shachar, M., Lüdtke, D. . bayestestR: Describing Effects and their Uncertainty, Existence and Significance within the Bayesian Framework. *Journal of Open Source Software* 2019;**4**(40):1581 doi 10.21105/joss.01541.
38. Gelman A, Rubin, D.B. Inference from iterative simulation using multiple sequences. *Sci Rep* 1992;**7**(4):457-72
39. Flegal JM, Haran, M., Jones, G.L. . . Markov chain Monte Carlo: Can we trust the third significant figure? *Statist Sci* 2008;**23**(2):250-60
40. Rizopoulos D, Hatfield, L., Carlin, B., Takkenberg, J. . Combining Dynamic Predictions from Joint Models for Longitudinal and Time-to-Event Data Using Bayesian Model Averaging. *Journal of the American Statistical Association* 2014;**109**:1385–97.
41. Wang H, Li G. A Selective Review on Random Survival Forests for High Dimensional Data. *Quant Biosci* 2017;**36**(2):85-96 doi 10.22283/qbs.2017.36.2.85.
42. Ishwaran H, Kogalur UB, Blackstone EH, Lauer MS. Random Survival Forests. *Ann Appl Stat* 2008;**2**(3):841-60 doi 10.1214/08-Aoas169.
43. Chen PL, Roh W, Reuben A, Cooper ZA, Spencer CN, Prieto PA, *et al.* Analysis of Immune Signatures in Longitudinal Tumor Samples Yields Insight into Biomarkers of Response and Mechanisms of Resistance to Immune Checkpoint Blockade. *Cancer Discov* 2016;**6**(8):827-37 doi 10.1158/2159-8290.CD-15-1545.
44. Carstens JL, Correa de Sampaio P, Yang D, Barua S, Wang H, Rao A, *et al.* Spatial computation of intratumoral T cells correlates with survival of patients with pancreatic cancer. *Nat Commun* 2017;**8**:15095 doi 10.1038/ncomms15095.
45. Liu CX, Musco S, Lisitsina NM, Forgacs E, Minna JD, Lisitsyn NA. LRP-DIT, a putative endocytic receptor gene, is frequently inactivated in non-small cell lung cancer cell lines. *Cancer Res* 2000;**60**(7):1961-7.
46. Chen H, Chong W, Wu Q, Yao Y, Mao M, Wang X. Corrigendum: Association of LRP1B Mutation With Tumor Mutation Burden and Outcomes in Melanoma and Non-small Cell Lung Cancer Patients Treated With Immune Check-Point Blockades. *Front Immunol* 2019;**10**:1523 doi 10.3389/fimmu.2019.01523.

47. Lam VK, Zhang J. Blood-based tumor mutation burden: continued progress toward personalizing immunotherapy in non-small cell lung cancer. *J Thorac Dis* 2019;**11**(6):2208-11 doi 10.21037/jtd.2019.05.68.
48. Hui E, Cheung J, Zhu J, Su X, Taylor MJ, Wallweber HA, *et al.* T cell costimulatory receptor CD28 is a primary target for PD-1-mediated inhibition. *Science* 2017;**355**(6332):1428-33 doi 10.1126/science.aaf1292.
49. Cristescu R, Mogg R, Ayers M, Albright A, Murphy E, Yearley J, *et al.* Pan-tumor genomic biomarkers for PD-1 checkpoint blockade-based immunotherapy. *Science* 2018;**362**(6411) doi 10.1126/science.aar3593.
50. Hsu CL, Ou DL, Bai LY, Chen CW, Lin L, Huang SF, *et al.* Exploring Markers of Exhausted CD8 T Cells to Predict Response to Immune Checkpoint Inhibitor Therapy for Hepatocellular Carcinoma. *Liver Cancer* 2021;**10**(4):346-59 doi 10.1159/000515305.
51. Miller BC, Sen DR, Al Abosy R, Bi K, Virkud YV, LaFleur MW, *et al.* Subsets of exhausted CD8(+) T cells differentially mediate tumor control and respond to checkpoint blockade. *Nat Immunol* 2019;**20**(3):326-36 doi 10.1038/s41590-019-0312-6.
52. Reuben A, Gittelman R, Gao J, Zhang J, Yusko EC, Wu CJ, *et al.* TCR Repertoire Intratumor Heterogeneity in Localized Lung Adenocarcinomas: An Association with Predicted Neoantigen Heterogeneity and Postsurgical Recurrence. *Cancer Discov* 2017;**7**(10):1088-97 doi 10.1158/2159-8290.CD-17-0256.
53. Chen R, Lee WC, Fujimoto J, Li J, Hu X, Mehran R, *et al.* Evolution of Genomic and T-cell Repertoire Heterogeneity of Malignant Pleural Mesothelioma Under Dasatinib Treatment. *Clin Cancer Res* 2020;**26**(20):5477-86 doi 10.1158/1078-0432.CCR-20-1767.
54. Bocchialini G, Lagrasta C, Madeddu D, Mazzaschi G, Marturano D, Sogni F, *et al.* Spatial architecture of tumour-infiltrating lymphocytes as a prognostic parameter in resected non-small-cell lung cancer. *Eur J Cardiothorac Surg* 2020;**58**(3):619-28 doi 10.1093/ejcts/ezaa098.
55. Hu X, Fujimoto J, Ying L, Fukuoka J, Ashizawa K, Sun W, *et al.* Multi-region exome sequencing reveals genomic evolution from preneoplasia to lung adenocarcinoma. *Nat Commun* 2019;**10**(1):2978 doi 10.1038/s41467-019-10877-8.
56. Chen M, Chen R, Jin Y, Li J, Hu X, Zhang J, *et al.* Cold and heterogeneous T cell repertoire is associated with copy number aberrations and loss of immune genes in small-cell lung cancer. *Nat Commun* 2021;**12**(1):6655 doi 10.1038/s41467-021-26821-8.
57. Dejima H, Hu X, Chen R, Zhang J, Fujimoto J, Parra ER, *et al.* Immune evolution from preneoplasia to invasive lung adenocarcinomas and underlying molecular features. *Nat Commun* 2021;**12**(1):2722 doi 10.1038/s41467-021-22890-x.
58. Lee WC, Reuben A, Hu X, McGranahan N, Chen R, Jalali A, *et al.* Multiomics profiling of primary lung cancers and distant metastases reveals immunosuppression as a common characteristic of tumor cells with metastatic plasticity. *Genome Biol* 2020;**21**(1):271 doi 10.1186/s13059-020-02175-0.
59. Feng C, Ding G, Ding Q, Wen H. Overexpression of low density lipoprotein receptor-related protein 1 (LRP1) is associated with worsened prognosis and decreased cancer immunity in clear-cell renal cell carcinoma. *Biochem Biophys Res Commun* 2018;**503**(3):1537-43 doi 10.1016/j.bbrc.2018.07.076.
60. Wang M, Xiong Z. The Mutation and Expression Level of LRP1B are Associated with Immune Infiltration and Prognosis in Hepatocellular Carcinoma. *Int J Gen Med* 2021;**14**:6343-58 doi 10.2147/IJGM.S333390.
61. Nong J, Gong Y, Guan Y, Yi X, Yi Y, Chang L, *et al.* Author Correction: Circulating tumor DNA analysis depicts subclonal architecture and genomic evolution of small cell lung cancer. *Nat Commun* 2019;**10**(1):552 doi 10.1038/s41467-019-08570-x.
62. Ma F, Guan Y, Yi Z, Chang L, Li Q, Chen S, *et al.* Assessing tumor heterogeneity using ctDNA to predict and monitor therapeutic response in metastatic breast cancer. *Int J Cancer* 2020;**146**(5):1359-68 doi 10.1002/ijc.32536.

63. Leader AM, Grout JA, Maier BB, Nabet BY, Park MD, Tabachnikova A, *et al.* Single-cell analysis of human non-small cell lung cancer lesions refines tumor classification and patient stratification. *Cancer Cell* 2021;**39**(12):1594-609 e12 doi 10.1016/j.ccell.2021.10.009.
64. House IG, Savas P, Lai J, Chen AXY, Oliver AJ, Teo ZL, *et al.* Macrophage-Derived CXCL9 and CXCL10 Are Required for Antitumor Immune Responses Following Immune Checkpoint Blockade. *Clin Cancer Res* 2020;**26**(2):487-504 doi 10.1158/1078-0432.CCR-19-1868.
65. Im SJ, Hashimoto M, Gerner MY, Lee J, Kissick HT, Burger MC, *et al.* Defining CD8+ T cells that provide the proliferative burst after PD-1 therapy. *Nature* 2016;**537**(7620):417-21 doi 10.1038/nature19330.
66. Siddiqui I, Schaeuble K, Chennupati V, Fuertes Marraco SA, Calderon-Copete S, Pais Ferreira D, *et al.* Intratumoral Tcf1(+)PD-1(+)CD8(+) T Cells with Stem-like Properties Promote Tumor Control in Response to Vaccination and Checkpoint Blockade Immunotherapy. *Immunity* 2019;**50**(1):195-211 e10 doi 10.1016/j.immuni.2018.12.021.

Table 1. Associations of genes with outcomes by arm using NanoString.

Arm	Gene	Outcome	HR	CI	P
nivo	FADD	OS	3.63	1.32-9.93	0.002
	CLEC4C	OS	3.06	1.16-8.09	0.009
	DNAJC14	OS	2.96	1.13-7.79	0.010
	CREB5	PFS	4.04	1.41-11.56	<0.001
	FADD	PFS	2.79	1.08-7.19	0.007
	IL-19	PFS	2.65	1.04-6.75	0.009
	PIN1	PFS	0.36	0.15-0.90	0.005
nivo+ipi	CCL22	OS	4.26	1.16-15.66	0.006
	CD163	OS	0.21	0.06-0.71	0.007
	CXCL10	OS	0.22	0.06-0.74	0.009
	CXCL11	OS	0.22	0.06-0.74	0.009
	IFI27	OS	0.22	0.07-0.76	0.010
	ITGB3	OS	0.17	0.05-0.62	0.002
	MAPK11	OS	4.48	1.20-16.68	0.004
	MAPK8	OS	0.19	0.06-0.67	0.004
	C1R	PFS	0.22	0.07-0.75	0.010
	C1S	PFS	0.21	0.06-0.71	0.007
	CD163	PFS	0.18	0.05-0.64	0.002
	ETS1	PFS	0.19	0.06-0.67	0.004
	FCGR2A	PFS	0.20	0.06-0.69	0.004
	IL15RA	PFS	0.22	0.07-0.75	0.010
	IL-32	PFS	0.19	0.06-0.67	0.004
	ITGB3	PFS	0.17	0.05-0.60	0.001
	MAPK8	PFS	0.20	0.06-0.71	0.006
PRKCD	PFS	0.19	0.05-0.66	0.004	
STAT2	PFS	0.22	0.06-0.74	0.009	

nivo, nivolumab; nivo+ipi, nivolumab plus ipilimumab; OS, overall survival; PFS, progression-free survival

Table 2. Associations between cell phenotypes by compartment and by treatment arm.

Arm	Compartment	Cell phenotype	Outcome	HR	CI	P
nivo+ipi	Tumor	CD3+CD8+GZB+	PFS	0.38	0.18-0.81	0.015
	Total	CD3+CD8-FOXP3+	OS	2.33	0.99-5.51	0.042
		CD3+PD-1+	PFS	0.45	0.21-0.97	0.035
nivo	Stroma	CD3+CD45RO+FOXP3+	PFS	0.58	0.32-1.05	0.049
	Total	CD3+CD45RO+	PFS	0.55	0.31-1.00	0.028
		CD3+CD45RO+FOXP3+	OS	0.52	0.28-0.96	0.026
		CD3+CD45RO+FOXP3+	PFS	0.42	0.23-0.78	<0.001

nivo, nivolumab; nivo+ipi, nivolumab plus ipilimumab; GZB, granzyme B; Total, tumor plus stroma; PFS, progression-free survival.

FIGURE LEGENDS

Figure 1. Kaplan-Meier survival curves of cellular densities and immune signatures. In the nivo arm (A-C), Kaplan-Meier survival curves show high cellular densities (> the median value used as cutoff) of (A) memory T cells (CD3+CD45RO+) in the total compartment and (B) CD45RO+ regulatory T cells (Tregs; CD3+CD45RO+FOXP3+) in the stroma compartment were associated with better progression-free survival (PFS). (C) CD45RO+ Tregs (CD3+CD45RO+FOXP3+) in the total compartment were associated with better OS. Representative multispectral images show low and high cell phenotype densities for A-C. In the nivo+ipi arm (D-F), the Kaplan-Meier survival curves show that high cellular densities of (D) PD-1+ T cells (CD3+PD-1+) in the total compartment and (E) GZB+ cytotoxic T cells (CD3+CD8+GZB+) in the total compartment were associated with better PFS. Conversely, (F) Tregs (CD3+CD8-FOXP3+) in the total compartment were associated with poor OS. Representative multispectral images show low and high cell phenotype densities for D-F. Cell scoring derived from gene expression profiling using nSolver shows higher scores for (G) CD45+ immune cells, (H) CD8+ T cells, and (I) neutrophils in responders compared with nonresponders in the nivo+ipi arm.

Figure 2. Immune infiltration in exceptional responders and early progression across the arms. (A) The upper level of the event chart shows the exceptional responders, and the lower level shows the early progression/death group. The solid red circles represent deaths in the overall survival (OS) analysis, the open red circles indicate OS-censored patients, the solid blue triangles indicate progression in the progression-free survival (PFS) analysis, the open blue triangles indicate PFS-censored patients, and the violet X indicates the time to the first response. Representative multispectral images of panels 1 (B) and 2 (C) show high levels of inflammatory cells in a sample from an exceptional responder patient. (D) Box plot shows GZB+ cytotoxic T cells (CD3+CD8+GZB+) in patients with exceptional response compared to patients with early progression/death. Representative multispectral images of panels 1 (E) and 2 (F) show reduced immune infiltration in a progression/death patient sample. (G) The spatial organization of immune and malignant cell phenotypes for the two mIF panels is shown with an example each from exceptional responders and early progressors. The colors for the different sub-populations are indicated under panel phenotype legend (on the left). (H) For the above images, segregation

of different cell phenotypes based on their spatially varying probabilities is shown as a contour plot. The colors of different neighborhoods is same as the panel phenotypes (above). **(I)** For the above images, Euclidean distance based clusters of cells (10 or more) within 20 microns are identified. The clusters are represented by numbers and distinct colors. **(J)** The relative percentage composition of cell types within each cluster (above) is indicated in the heatmap. The corresponding cluster colors are indicated below the heatmap for reference. The color scale representing percentage composition (0-100), is shown on the left.

Figure 3. Kaplan-Meier survival curves of nearest neighbor distance from both arms. **(A)** Upper and lower image showing proximity map overlay, where cyan dots represent malignant cells (CK+) and red dots represent T cells (CD3+). White lines display distances from all malignant cells (CK+) to neighboring T cells (CD3+). **(B-E)** Kaplan-Meier survival curves show that distances (\leq the median value used as cutoff) from **(B)** malignant cells (CK+) to cytotoxic T cells (CD3+CD8+) and **(C)** GZB+ cytotoxic T cells (CD3+CD8+GZB+) and **(D)** malignant cells expressing PD-L1 (CK+PD-L1) to cytotoxic T cells (CD3+CD8+) were associated with better progression-free survival (PFS) when combining both treatment arms. **(E)** Kaplan-Meier OS curve for distances from malignant (CK+) to GZB+ cytotoxic T cells (CD3+CD8+GZB+) in both arms. In the nivo+ipi arm **(F-I)**, Kaplan-Meier survival curves show that close distances (\leq the median value used as cutoff) from **(F)** malignant cells (CK+) to cytotoxic T cells (CD3+CD8+) and **(G)** GZB+ cytotoxic T cells (CD3+CD8+GZB+), and **(H)** PD-L1+ malignant cells (CK+PD-L1+) to cytotoxic T cells (CD3+CD8+) were associated with better PFS. **(I)** Close distances from malignant cells (CK+) to GZB+ cytotoxic T cells (CD3+CD8+GZB+) was associated with OS.

Figure 4. Olink serum soluble analyte assessment. **(A)** Heatmap of dynamic changes in protein expression. The *x*-axis shows the protein names, while the *y*-axis shows the comparisons between timepoints and progression. The color represents the logFC. Green represents increase from baseline while pink represents decrease. The size of the circle indicates the statistical significance expressed as $-\log_{10}(\text{FDR})$. **(B)** Boxplots and median red lines showing the expression over time by cohort for CXCL9 and CXCL13. **(C)** Heatmap for differential protein expression between responders and nonresponders. The *x*-axis shows the protein names, while

the y-axis shows each timepoint. The symbol in the heatmap represents the statistical significance: circles for $FDR < 0.05$ or adjusted P values, squares for $P < 0.05$, and triangles for nonsignificant or $P > 0.05$. The color represents the change relative to upregulation in responders (blue) or nonresponders (red). **(D)** Boxplots corresponding to significant markers in C over time, stratified by treatment arm for the indicated proteins. Comparisons for individual baseline, cycle 2, and cycle 4 timepoints are shown for $P < 0.05$ and $FDR < 0.05$ with (*) and (**), respectively. **(E)** Heatmap showing the concordance in directionally of differentially expressed proteins significant between exceptional responders and all responders. The direction of the protein changes was identical between both groups of responders, but only CXCL13 and CCL23 reached statistical significance (FDR, darker colors) for exceptional responders due the decreased numbers. Nominal significance is shown as transparent colors, indicating proteins with $P < 0.05$. **(F)** Volcano plot showing the proteins significantly associated with overall survival (OS) when jointly modeling cytokine expression over time. The proteins labeled in blue are associated with increased hazard ratio or decreased survival. Kaplan-Meier OS curves for CSF-1, IL-8, CXCL13 and MMP12 stratified based on their expression from the average expression (higher values from the mean as blue, lower values from the mean as red).

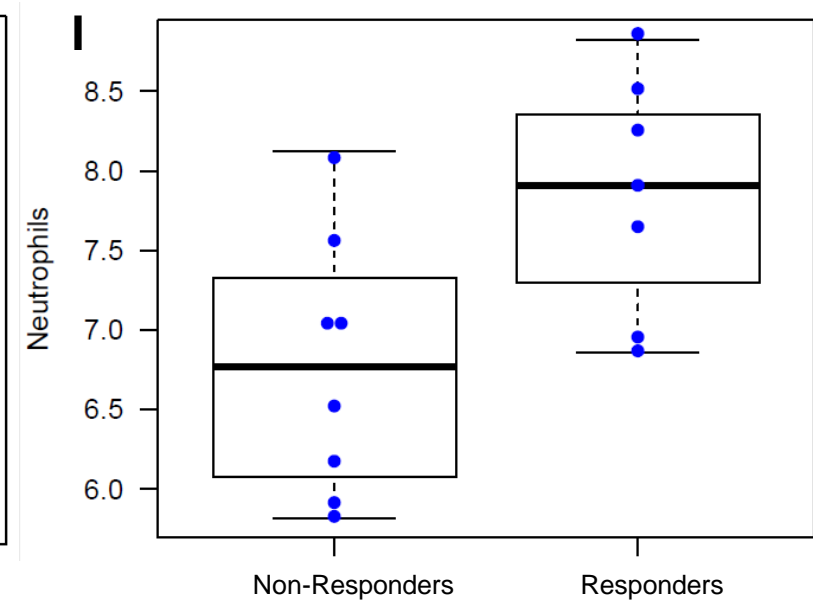
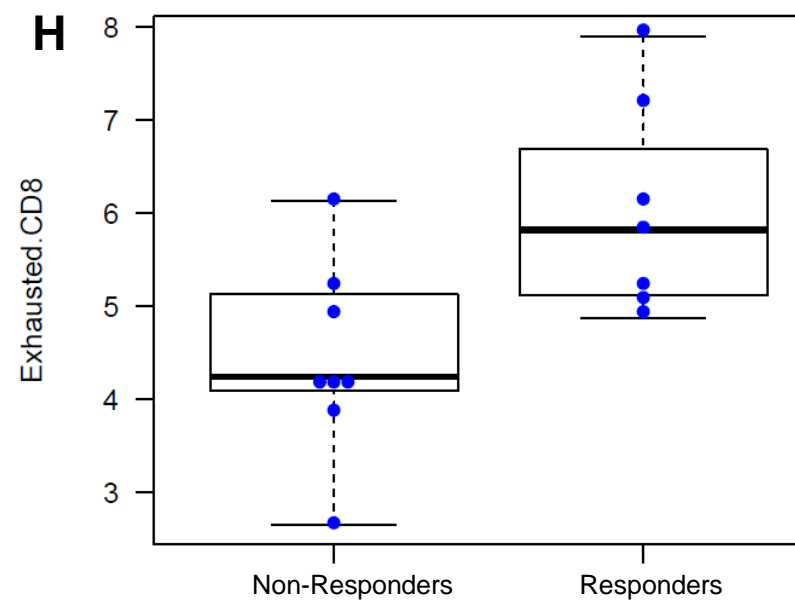
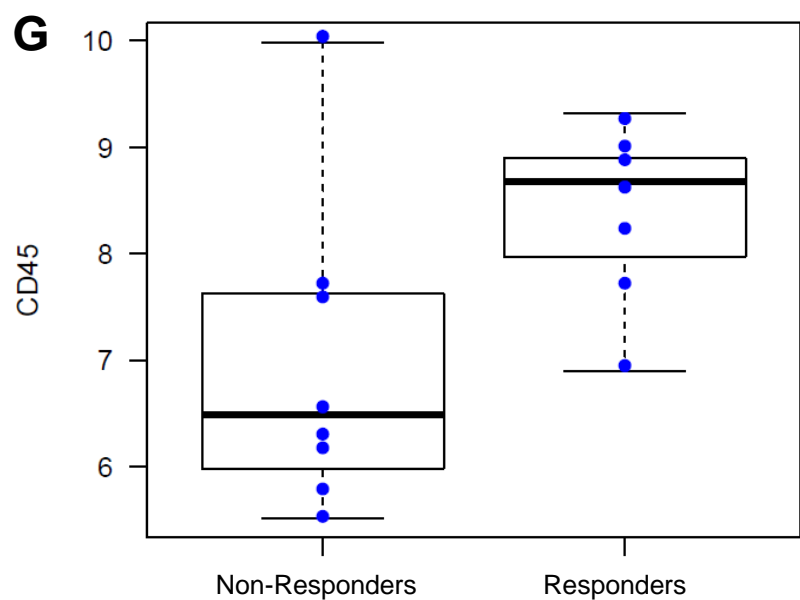
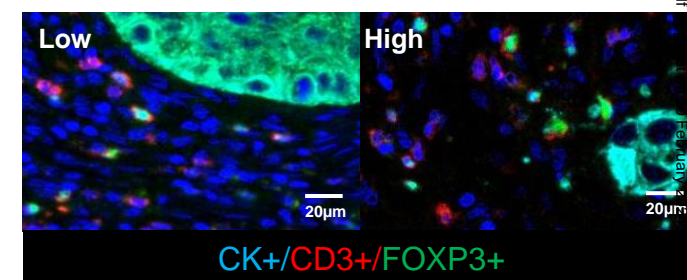
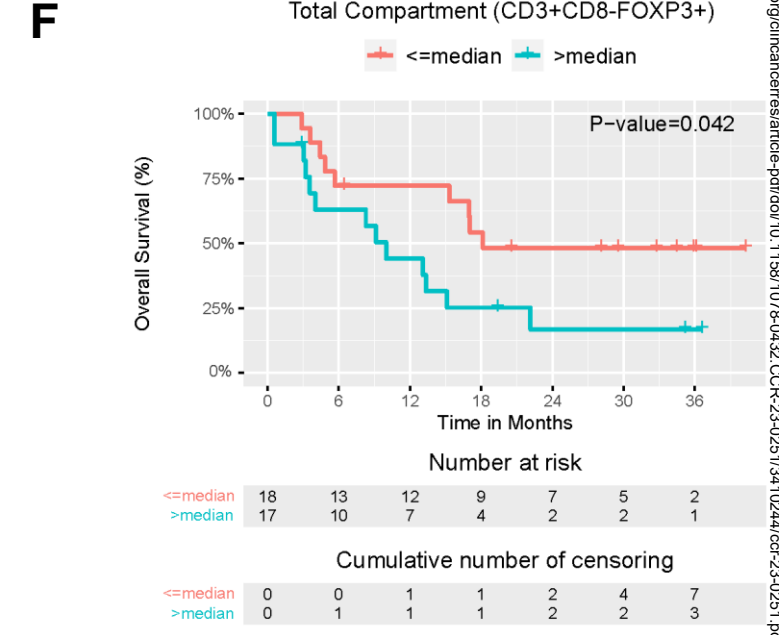
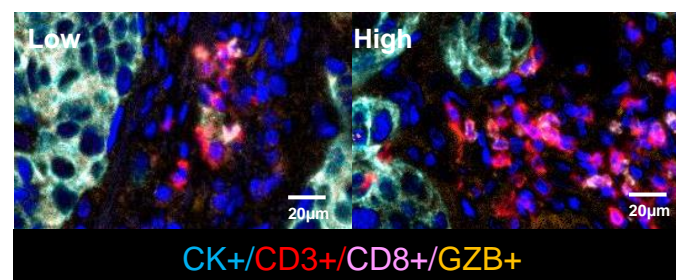
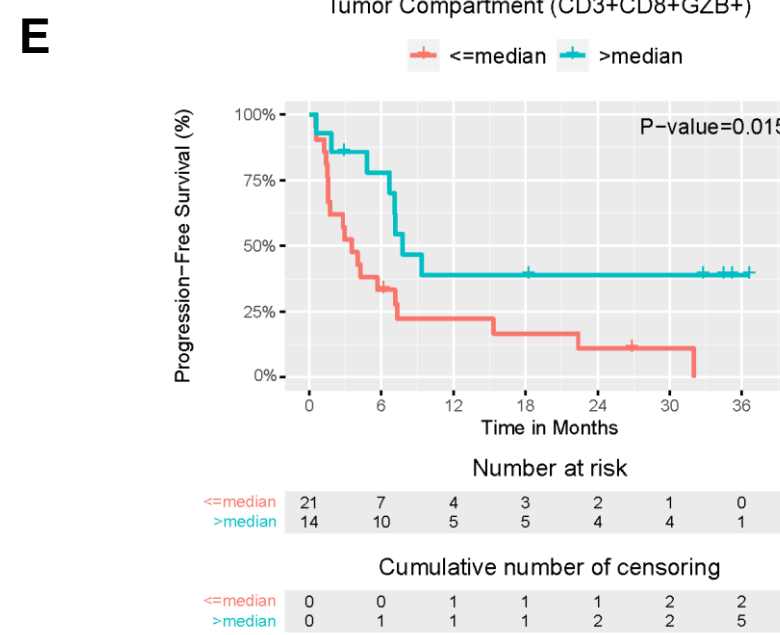
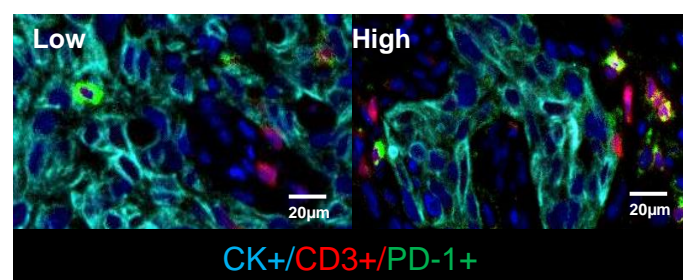
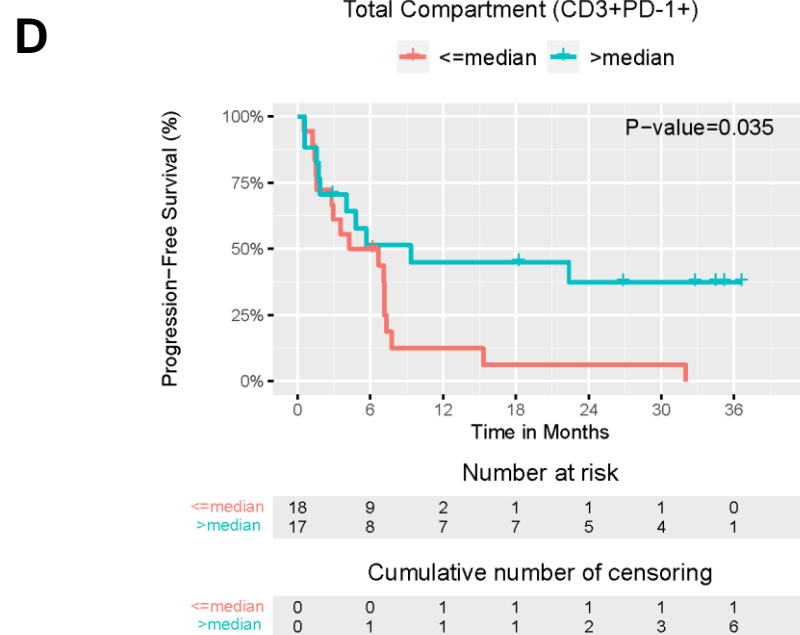
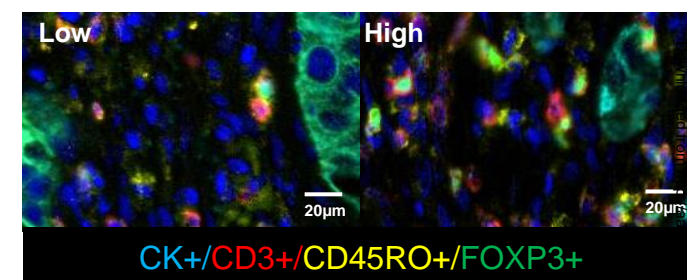
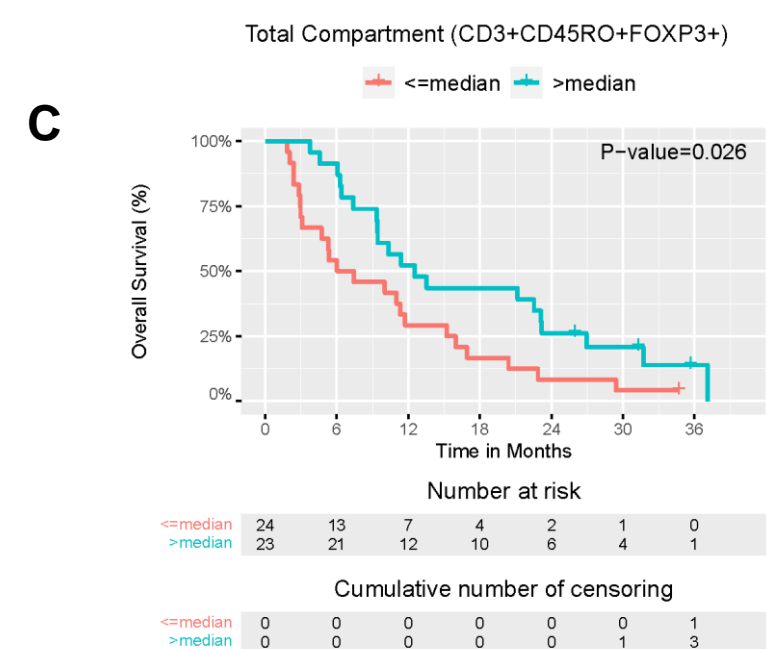
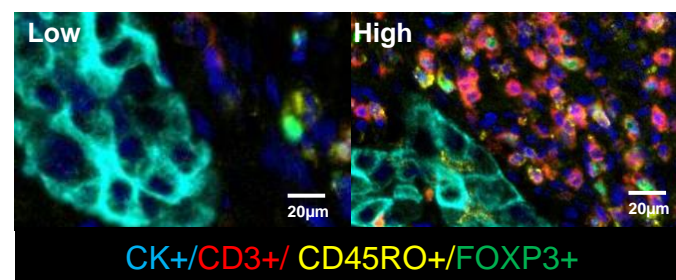
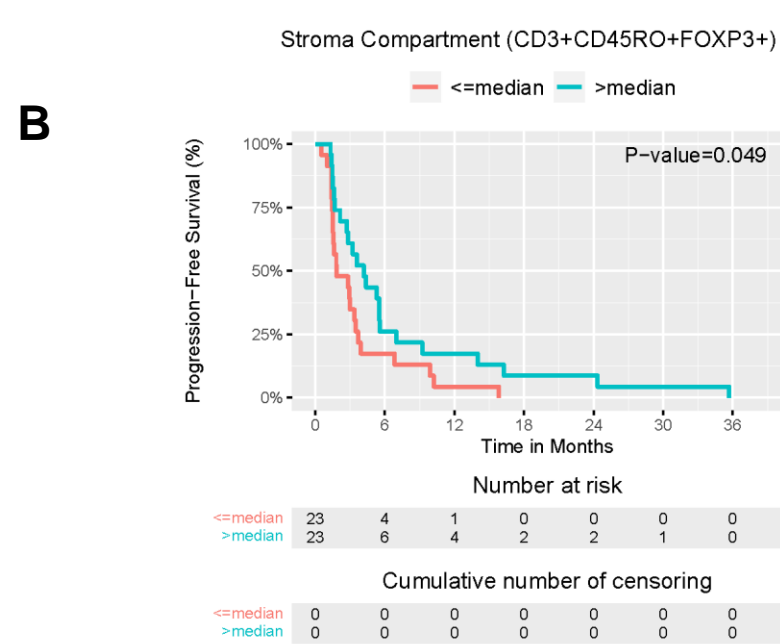
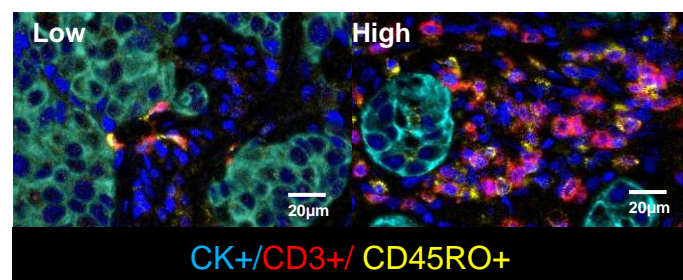
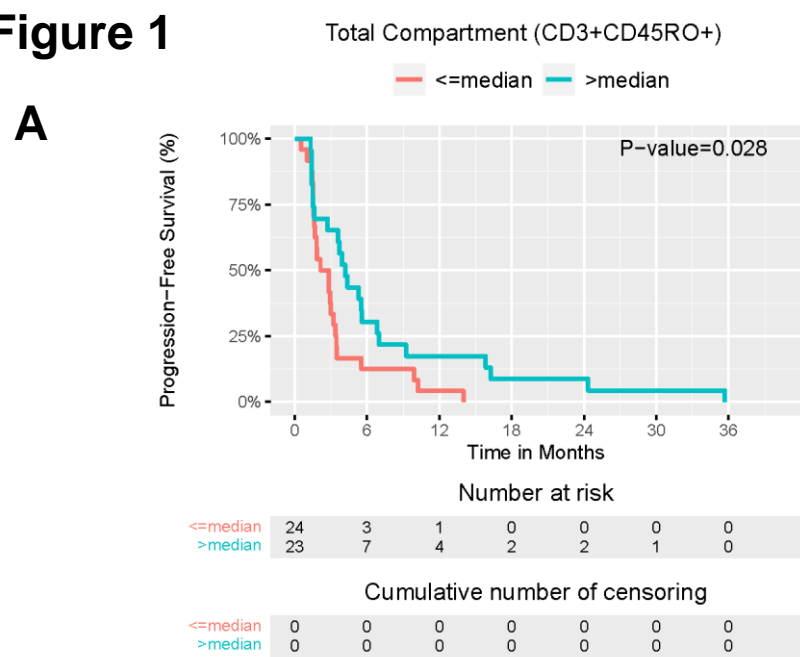
Figure 1

Figure 2

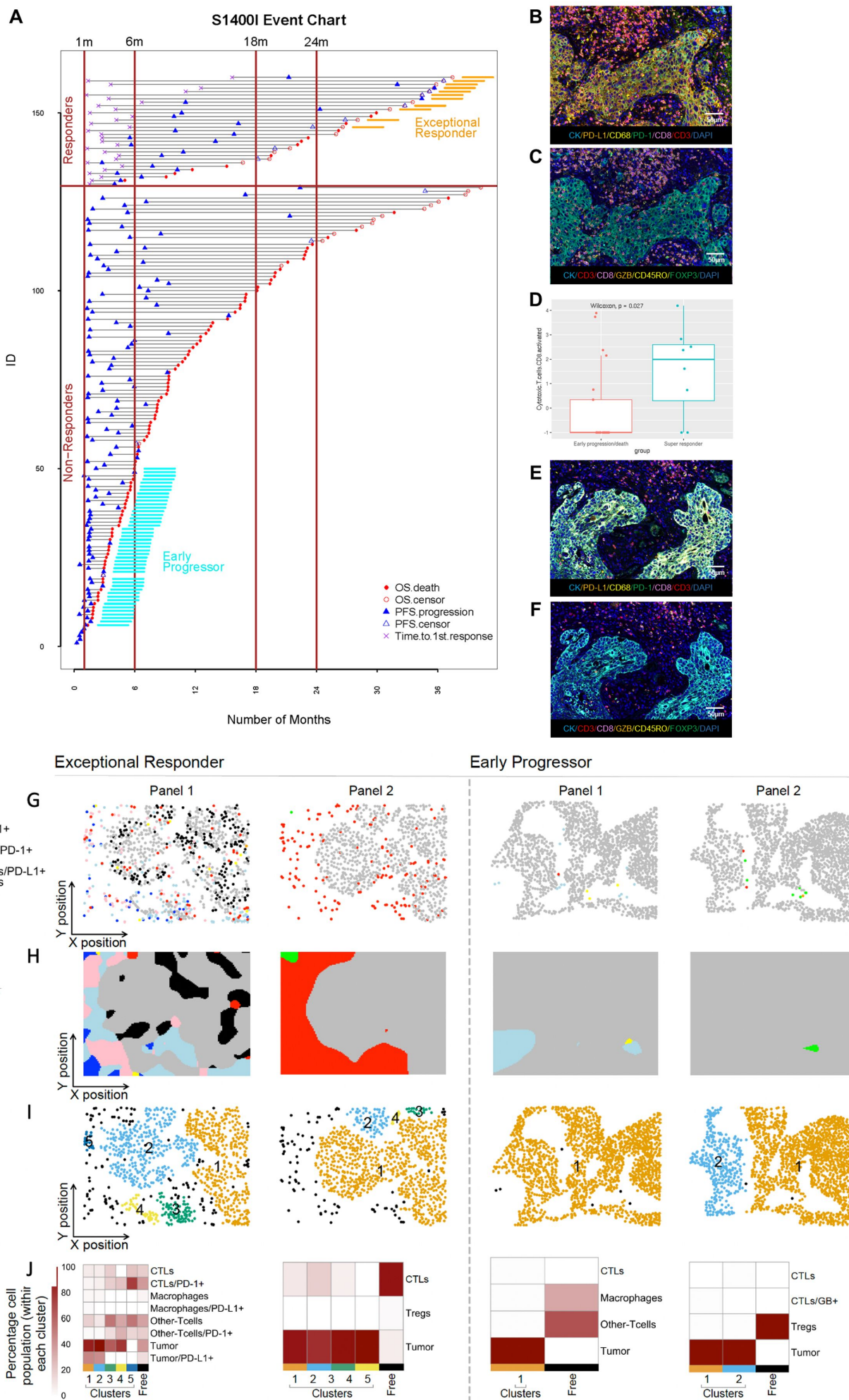


Figure 3

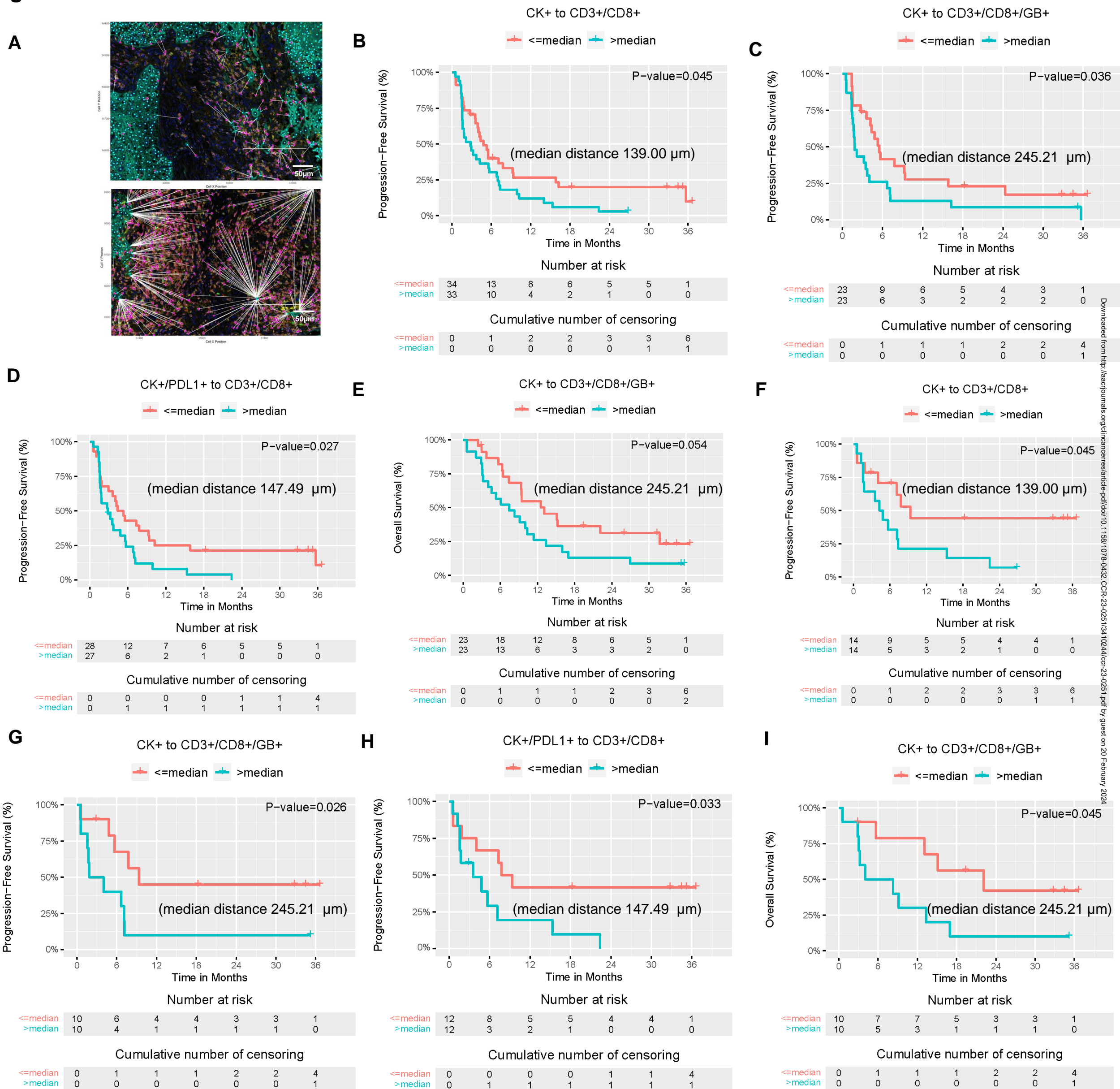


Figure 4

